SHAPE OPTIMIZATION IN HIGH-SPEED HYDRO- AND AERODYNAMICS TO PREVENT SEPARATION AND CAVITATION

I. Nesteruk

Institute of Hydromechanics NASU, Kyiv, Ukraine

inesteruk@yahoo.com

ABSTRACT

The volumetric pressure drag for the standard supercavitating bodies (such as disc or cone) and for the cavitators with curvature was estimated. Analytic formulas for the skin-friction drag of the unseparated slender axisymmetric shapes are presented. It was shown that the main reserve of the drag reduction consists in using shapes providing the unseparated flow pattern.

The volumetric drag coefficients for supercavitating and unseparated flow patterns were compared. It was shown that the standard supercavitating flow pattern is preferable for smaller values of the volumetric Reynolds number $\mathrm{Re}_V < 10^7$ only. The cavitation number has to be close to minimal possible value $\sigma \approx 0.01$. Some efficiency comparison is also presented for the unsteady movement on inertia. I was shown, for supercavitating flow pattern the maximum range be achieved with the use of special shapes of the bodies located in the cavity. These shapes are different for different isoperimetric conditions, but for large Reynolds numbers the unseparated bodies are preferable.

In order to achieve the flow pattern without separation and cavitation the special shaping only was used. The presented unseparated shapes allow reducing the drag and the noise without any additional energy supply, since there is no need in using active boundary-layer control methods (such as suction, blowing or heating). They can be used in water and as well in air. Theoretical and experimental results concerning the axisymmetric unseparated bodies are presented. 2D airfoils with negative pressure gradients over the surface are calculated. Examples of sub- and supersonic axisymmetric shapes without separation are presented. The presented unseparated shapes could be also use to prevent cavitation or to improve the cavitation inception characteristics.

Keywords: Drag reduction, supercavitation, separation, optimization.

1. INTRODUCTION

The Ryabushinsky flow pattern, shown in Fig. 1, could be the best one for drag diminishing in high-speed hydrodynamics. Really, according to the Dalambert paradox, such rigid body could have near to zero pressure drag, and due to the great area wetted by gas instead of water in the region $0 < x < L$, the friction drag could be sufficiently reduced. Unfortunately, instabilities in flow and gravity forces deform the cavity shape in such a way, that it cannot reattach to the rigid body in the region $x > L$. Therefore, it is impossible to realize the flow
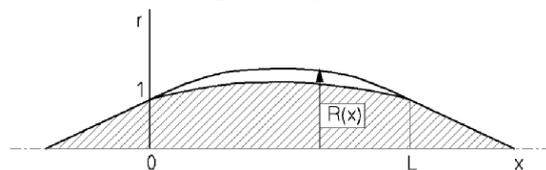

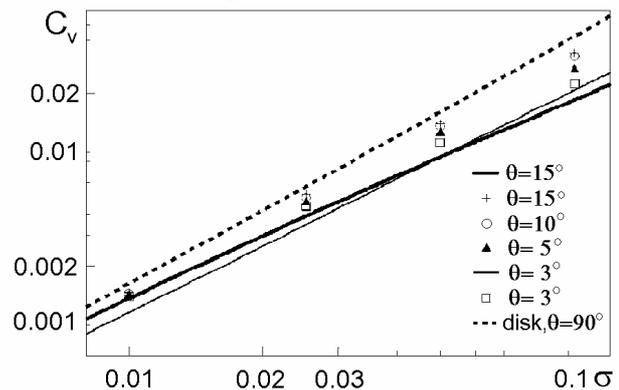**Fig. 1. The Ryabushinsky flow pattern with zero pressure drag**

Fig. 2. Volumetric drag coefficients for cones.

pattern shown in Fig. 1, the rear part of the cavity is unsteady and two-phase, and pressure drag occurs, since the pressure on the cavitator $x < L$ is not compensated by the pressure on the closer part $x > L$. The estimations of the pressure drag for conic and disc cavitators and for cavitators with curvature are presented in Section 2.

An alternative to the supercavitating flow pattern with a small cavitator and long body located in the cavity is the shape without separation. Unseparated body has zero pressure drag, but its entire surface is wetted by liquid, therefore, its friction drag can be very high in comparison with the supercavitating flow pattern. To compare these alternatives the experimental data and drag estimations for axisymmetric bodies are analyzed in Section 3. Analytic formulas for the skin-friction drag of the unseparated slender axisymmetric shapes are presented in Section 4. It was shown that the main reserve of the drag reduction consists in using shapes providing the unseparated flow pattern.

In Section 5 the volumetric drag coefficients for supercavitating and unseparated flow patterns was compared. It was shown that the standard supercavitating flow pattern is preferable for smaller values of the volumetric Reynolds number $\mathrm{Re}_V < 10^7$ only. The cavitation number has to be close to minimal possible value $\sigma \approx 0.01$. Some efficiency comparison is also presented for the unsteady movement on inertia. I was shown, for supercavitating flow pattern the maximum range be achieved with the use of special shapes of the bodies located in the cavity. These shapes are different for different isoperimetric conditions, but for large Reynolds numbers the unseparated bodies are preferable.

Very important question: have to obtain the shape without separation, is discussed in Section 6. The presented unseparated shapes allow reducing the drag and the noise without any additional energy supply, since there is no need in using active boundary-layer control methods (such as suction, blowing or heating). They can be used in water and as well in air. Theoretical and experimental results concerning the axisymmetric unseparated bodies are presented in Section 6. 2D airfoils with negative pressure gradients over the surface and examples of sub- and supersonic axisymmetric shapes without separation are presented in Section 6.

The presented unseparated shapes could be also use to prevent cavitation or to improve the cavitation inception characteristics. This question is discussed in Section 7.

2. VOLUMETRIC PRESSURE DRAG COEFFICIENTS OF STANDARD CAVITATORS

For the standard axisymmetric supercavitating bodies (located in cavities after a disc or a cone) the main part of the drag D is connected with the pressure drag of the cavitator. In [1] the following formula was obtained:

$$C_V = \sqrt[3]{\frac{9\pi\sigma^4}{-16\ln\sigma}} \qquad (2.1)$$

for conic cavitators with the angle 2θ, $\theta > 25^0$. It must be noted that the value C_V does not depend on θ for these non-slender cavitators and tends to zero with diminishing of the cavitation number σ. The relationship (2.1) represented in Fig. 2 by the dashed line. The results of non-linear numerical calculations for slender cones with the use of the paper [2] method are presented by dots. The linear calculations with the use of formulas from [3] are shown in Fig.2 by solid lines.

The cavitation number cannot be diminished to zero, since the appropriate cavity slenderness ratio $\varepsilon = R_{\max} / L$ also tends to zero for $\sigma \to 0$. The same value of ε has also the body part located in the cavity. Constructive considerations restrict the body slenderness ratio. For example, Savchenko the following limiting value $\varepsilon \geq 0.025$ has proposed, which leads to

the restrictions $\sigma \geq 0.01$ for the disc cavitator and $C_V \geq 1.5 \cdot 10^{-3}$ for all standard conical cavitators (see Fig.2).

The influence of the cavitator shape curvature on the pressure drag coefficient was investigated in [4]. The drag coefficients of the concave and the convex cavitators with different values of the curvature parameter b and the derivative of the radius β were calculated. The comparison of the volumetric pressure drag coefficients showed, that the smallest ones correspond to the concave shapes, but the difference in C_V of these cavitators and conical ones can be neglected. Therefore, the minimal possible value of C_V for the cavitators with curvature remains the same and is approximately $1.5 \cdot 10^{-3}$.

3. EXPERIMENTAL DATA AND DRAG ESTIMATIONS FOR SUBSONIC AXISYMMETRIC BODIES

Shapes of revolution are of great practical interest, since they are the first approximation for airplane hulls and underwater vehicles. The experimental data concerning the total drag of subsonic axisymmetric bodies are rather scattered (see [5,6]). Hoerner noted that the drag coefficients of two bodies having the same fineness ratio might be different in the ratio of 1 to 2 at the same Reynolds number. He explains this fact by the influence of the body support and the boundary-layer transition, which is a complex function of shape, Reynolds number and stream turbulence. Nevertheless, Hoerner proposed two formulae for the total drag coefficient in laminar and turbulent cases, [6]]:

$$C_{dS} = C_{fl}\left[1 + 1.5(D/L)^{1.5}\right] + 0.11(D/L)^2, \qquad (3.1)$$

$$C_{dS} = C_{ft}\left[1 + 1.5(D/L)^{1.5} + 7(D/L)^3\right], \qquad (3.2)$$

$$C_{fl} = \frac{1.328}{\sqrt{\mathrm{Re}_L}}, \qquad C_{ft} = \frac{0.0307}{\mathrm{Re}_L^{1/7}}. \qquad (3.3)$$

Here C_{dS} is based on the wetted area S, D and L are the maximum body diameter and its length, C_{fl} and C_{ft} are plane plate skin-friction coefficients obtained by Blasius for the laminar flow and by Falkner for the turbulent one (see, for example, [7]). Different drag coefficients and Reynolds numbers are defined as follows:

$$C_{dS} = \frac{2D}{\rho U_\infty^2 S}; \qquad C_{dL} = \frac{2D}{\rho U_\infty^2 L^2}; \qquad \mathrm{Re}_L = \frac{U_\infty L}{\nu}: \qquad \mathrm{Re}_V = \frac{U_\infty V^{1/3}}{\nu}.$$

It should be noted that for laminar flow the pressure drag C_{dp} (the drag component due to separation) is equal to $0.11(D/L)^2$ and independent from the Reynolds number. In the turbulent case, this drag component $7C_{ft}(D/L)^3$ depends on Re_L. Hoerner does not explain this fact reporting only that the pressure drag component in equation (3.2) was found statistically.

Formulae (3.1) and (3.2) may be applied to the body "Dolphin" manufactured and tested by North American Aviation in 1967-1968, see [5]. The profile NACA–66 was chosen for the shape of this body, its parameters were: L/D=3.33; D=0.48 m; L=1.6 m; $V = 0.159\,m^3$; $S = 1.69\,m^2$. The tests revealed the minimal value of $C_V = 0.008$ and $C_{dS} = 0.0014$ (at $\mathrm{Re}_L = 2.5 \cdot 10^7$). The theoretical estimation (3.1) yields the following value of $C_{dS} = 0.00027\left[1 + 0.246\right] + 0.01 \approx 0.01033$, which is more then 7 times greater as the experimental one. The main component of the drag is the pressure one, which exceeds the skin-friction in 30 times. In the turbulent case, equation (3.2) gives

$C_{dS} = 0.0027[1+0.246+0.189] \approx 0.0039$, which is approximately 3 times greater then the experimental value. In comparison with the formula (3.1), the pressure component is only 20% of the total drag and only 5% of its value for the laminar flow.

The great difference in values of C_{dp} for the laminar and turbulent cases is a contradiction. Probably, the term $0.11(D/L)^2$ in equation (3.1) is too large or/and the term $7C_{ft}(D/L)^3$ in formula (3.2) is too small. Another discrepancy is connected with the article [8], where axisymmetric shapes of minimal drag are calculated. The body optimized by Lutz and Wagner for $\mathrm{Re}_V = 0.85 \cdot 10^7$ has $C_{dV} \approx 0.02$, but the experimental value for the "Dolphin" is 2.5 times smaller.

4. SKIN-FRICTION DRAG OF SLENDER SUBSONIC AXISYMMETRIC BODIES

The main terms describing the friction in (3.1) and (3.2) are C_{fl} or C_{ft}, given by formulas (3.3). Both friction coefficients are obtained for plane plate. Nevertheless, the boundary layer on a slender axisymmetric body sufficiently differs from 2D one (see, for example, [9-11]). This fact can be proved with the use of Mangler-Stepanov transformations [7], which reduce the axisymmetric boundary-layer equations to a 2D case.

The relations between the coordinates x, y for the axisymmetric boundary-layer with the corresponding 2D coordinates $\bar{x}, \bar{y}$ has the following form, [7]:

$$\bar{x} = \int_0^x R^2(\xi)d\xi; \qquad \bar{y} = R(x)y . \tag{4.1}$$

Here $R(x)$ is the radius of the axisymmetric body. The flow velocity at the external scope of the boundary-layer, the displacement thickness and the skin-friction coefficient are related as follows (see [7]):

$$\bar{U} = U ; \qquad \delta^* = \frac{\bar{\delta}^*}{R(x)}; \qquad \tau_w = \bar{\tau}_w R(x) \tag{4.2}$$

Equations (4.1)-(4.3) are valid for an arbitrary axisymmetric body provides the thickness of the boundary layer is small in comparison with the radius.

For a slender axisymmetric body, the velocity U can be supposed to be approximately equal to 1.0, neglecting the thickness of the boundary layer and the pressure distribution peculiarities at the surface (see [12]). For the slender body, the coordinate x can also be calculated along the body's axis. According to the first formula (4.2), the value of $\bar{U}$ will be also equal to 1.0, i.e. within the chosen approach, the flat plate corresponds to the slender axisymmetric body.

Thus, the well-known results for the boundary layer on the plate may be used to estimate the skin–friction on the slender body of revolution. In particular, according to the Blasius formula for a laminar flow $\bar{\tau}_w = 0.664(\bar{x})^{-\frac{1}{2}} \mathrm{Re}_L^{-\frac{1}{2}}$. Introducing the variable x, in view of equations (4.1) and (4.2), the following formulae for the skin-friction coefficients of the slender axisymmetric body were obtained in [11]:

$$C_{dfL} = \frac{4.172}{\sqrt{\mathrm{Re}_L}} \int_0^1 R^2(x)[\int_0^x R^2(\xi)d\xi]^{-\frac{1}{2}} dx = 8.344\sqrt{\frac{V}{\pi L^3 \mathrm{Re}_L}} \sim \left(\frac{D}{L}\right)^2; \quad C_V = \frac{4.708}{\sqrt{\mathrm{Re}_V}}. \tag{4.3}$$

By means of the empirical Hoerner's formulas $V \approx 0.65 L\pi D^2/4$, $S \approx 0.75 L\pi D$, the skin-friction drag coefficient based on the wetted area can also be calculated

$$C_{dS} \approx \frac{1.43}{\sqrt{\mathrm{Re}_L}} \approx 1.075 C_{fl} \tag{4.4}$$

Thus, using the value 1.0 in formula (3.1) instead of 1.075 (according to equation (4.4)) does not lead to large discrepancy. Absolutely different situation takes place in the turbulent case, where the Falkner equation $\overline{\tau}_w = 0.0263(\overline{x})^{-1/7} \mathrm{Re}_L^{-1/7}$ (see [8]) yields the following formulae for the skin-friction drag:

$$C_{dfL} = 0.166\,\mathrm{Re}_L^{-1/7} \int_0^1 R^2(x)[\int_0^x R^2(\xi)d\xi]^{-1/7} dx = \frac{0.166\,W(1)}{\mathrm{Re}_L^{1/7}}; \qquad W(x) = \frac{7}{6}[\int_0^x R^2(\xi)d\xi]^{6/7}.$$

$$C_{dfL} = 0.0726\frac{V^{6/7}}{L^{18/7}\,\mathrm{Re}_L^{1/7}}; \quad C_{dfS} \approx 0.564 C_{ft}\left(\frac{D}{L}\right)^{5/7}; \quad C_V = 0.073\frac{V^{5/21}}{L^{15/21}\,\mathrm{Re}_V^{1/7}} \tag{4.5}$$

According to equation (4.5), the theoretical value of C_{dfS} is $0.564(D/L)^{5/7}$ times smaller then the value used in (3.2), i.e. the turbulent skin-friction drag in equation (3.2) seems to be too large (especially for slender bodies). Nevertheless, relatively good estimations of total drag can be obtained with the use of formula (3.2). For example, the shape "Dolphin" with the forced turbulence (by means of a small obstacle located in the boundary layer near the body's nose) revealed at $\mathrm{Re}_L = 1.8 \cdot 10^7$ the value $C_{dS} = 0.0034$, which is only 19% less then the estimation (3.2).

The contradiction can be eliminated by a redistribution of the skin-friction and pressure drag, i.e. the turbulent drag due to separation is larger then $7C_{ft}(D/L)^3$. In such way, in particular, can be explained the big difference in the pressure drag for equations (3.1) and (3.2) mentioned in Section 3.

The presented analysis allows one to draw a significant conclusion: **the main reserve of the drag reduction consists in using shapes providing the unseparated flow pattern.** For example, according to formula (4.5), the turbulent skin-friction coefficient $C_V = 0.0036$ at $\mathrm{Re}_V = 0.85 \cdot 10^7$ for the body "Dolphin". The experimental value $C_V = 0.008$ is twice greater due to the separation, therefore the drag can be diminished at least twice provides the shape of "Dolphin" would be unseparated.

It must be noted that in some cases turbulent and laminar skin-friction drag may be rather close. For example, equations (4.3) and (4.5) yield the values $C_{Vl} = 0.0032$ and $C_{Vt} \approx 0.0038$ at $\mathrm{Re}_V = 2.2 \cdot 10^6$ for the body of Hansen&Hoyt ([13], L/D=4.5; L=3.18 m; D=0.71 m). The experimental value $C_{dV} = 0.007$ testifies that with the use of an unseparated shape, the total drag might twice be reduced.

It should be noted that for the laminar flow the friction component of C_V is independent of the body shape and only depends on the volumetric Reynolds number (see (4.3)). In the turbulent case C_V is proportional to $(V/L^3)^{5/21} \sim (D/L)^{10/21}$ (see (4.5)). Therefore, slender forms with small values of the fineness ratio D/L must be used to minimize C_V.

This conclusion is supported with the results of [14], where airplanes hull with $D/L = 0.163$ was proposed. Nevertheless, the optimal shapes reported in [8] have a sufficiently higher fineness ratio. The theoretical values of the drag calculated in [8, 14, 15] are rather different. Probably, this can be explained by using different semi-empirical criterions of the laminar-turbulent transition in the boundary layer. The values of C_V calculated in [8, 14, 15]

exceed the estimation (4.5). For example, in [15] the theoretical value $C_V = 0.012$ at $\mathrm{Re}_V = 1.5 \cdot 10^7$ was obtained, whereas equation (4.5) yields $C_V = 0.0025$ at the same fineness ratio. The reason of this discrepancy probably is using the 2D boundary-layer characteristics without Mangler-Stepanov transformations in [8, 14, 15] .

5. DRAG COMPARISON FOR SUPERCAVITATING AND UNSEPARATED FLOW PATTERNS.   In this case the drag of the slender axisymmetric shapes is connected with the skin friction on the surface and C_V can be estimated with the use of formulas (4.3), (4.5) for the laminar and the turbulent boundary-layer respectively. It must be noted that in the laminar case C_V depends on the volumetric Reynolds number Re_V only and for $\mathrm{Re}_V > 10^7$ and $\varepsilon \le 0.025$ both formulas yield $C_V < 1.5 \cdot 10^{-3}$. Thus, the standard supercavitating flow pattern is preferable for smaller values of the volumetric Reynolds number $\mathrm{Re}_V < 10^7$ only. The cavitation number has to be close to minimal possible value $\sigma \approx 0.01$. For example, $C_V \approx 0.007$ for the non-cavitating underwater apparatus "Dolphin" measured at $\mathrm{Re}_V = 8.5 \cdot 10^6$, [16]. Therefore, for $\sigma > 0.03$ the supercavitation yields greater drag in comparison with the shape "Dolphin" (see Fig.2).

These conclusions call the effectiveness of the supercavitating body for Underwater Express Program (BAA06-13, Proposer Information Pamphlet (PIP)) in question, since the volumetric Reynolds numbers for the desired vehicle are greater than 10^8 for the desired vehicle. The conclusion: " Supercavitation offers 60-70% reduction in total drag on an underwater body", written in BAA06-13, Proposer Information Pamphlet (PIP) is not valid for large bodies (with large volumetric Reynolds numbers). A shape without separation could be more effective, if the unseparated flow pattern could be achieved. The perspectives of the unseparated bodies are discussed in Section 6.

If would be interesting to compare the effectiveness of the supercavitating and the unseparated bodies in the unsteady case as well. In particular, the underwater motion on inertia may be used for this purpose with the range as an effectiveness criterion. The supercavitating motion on inertia and the problem of range maximization were considered by Putilin [17], Gieseke [18], Serebriakov and other authors. Here the results of two recent papers [19, 20] will be presented.

Let the model start with the velocity U_0 under an arbitrary angle γ to horizon and then move in water on inertia. It was shown in [20] that in many cases the flow may be supposed as quasi-stationary, and the gravity effect on the cavity and body motion may be neglected and the known asymptotic relations by Garabedian, [28], may be used

$$R^2 = \frac{x(1-x)}{\lambda^2}, \qquad \frac{R_n}{L} = \frac{\sigma}{2\sqrt{-C_x \ln \sigma}}, \qquad \lambda = \frac{L}{D} = \sqrt{\frac{-\ln \sigma}{\sigma}}, \qquad \frac{D}{R_n} = 2\sqrt{\frac{C_x}{\sigma}} \qquad (5.1)$$

with the current cavitation number σ at the cavitator immersion depth. Here $R(x)$ is the cavity radius; R_n is the cavitator radius; λ is the cavity aspect ratio; D is the maximal cavity diameter; L is the cavity length; C_x is the cavitation drag coefficient related to the base section area of the cavitator πR_n^2. If we neglect changes of the cavitation number $\sigma \ll 1$, then C_x may be considered to be constant and the distance S passed by the body is defined by formula, [17]:

$$S = \frac{2m}{\rho C_x \pi R_n^2} \ln \frac{U_0}{U}, \qquad (5.2)$$

where m is the body mass; U is the final body velocity.

In [19, 20] formula (5.2) is analyzed for different isoperimetric conditions. Similar optimal problems were considered by Putilin, Gieseke, Serebriakov for the case of horizontal motion.

Taking into account that a body practically stops after washing off by water, it follows from (5.2) that the optimal body shape must coincide with the cavity shape in the moment of washing off (see also [17]). Then formulae (5.1) and (5.2) yield

$$\overline{S} \equiv \frac{S}{L} = -\frac{2\overline{\rho}_b Fr_0^2 \overline{U}^2 \ln \overline{U}}{3(\overline{h}_1 - \overline{S} \sin \gamma)}, \qquad (5.3)$$

where $\overline{U} = U / U_0$; $\overline{\rho}_b = m / V\rho$; V is the body volume; $\overline{h}_1 = (10 + h_0)/L$; h_0 is the initial depth of the cavitator; $Fr_0 = U_0 / \sqrt{gL}$ is the initial Froude number; γ is the angle of the trajectory to the horizon ($\gamma = 0$ for the horizontal motion, $\gamma > 0$ for the motion upwards).

For the fixed values of $\overline{\rho}_b, L, \gamma, h_0, U_0$ the maximal range depends on the final velocity U only. It follows from (5.3) that maximal range $\overline{S}_*$ corresponds to

$$\overline{U}_* = e^{-0.5} \approx 0.607, \qquad (5.4)$$

and is equal to

$$\overline{S}_* = \begin{cases} \dfrac{\overline{\rho}_b Fr_0^2}{3e\overline{h}_1}, & \gamma = 0, \\[3mm] \dfrac{3\overline{h}_1 - \sqrt{9\overline{h}_1^2 - 12\overline{\rho}_b Fr_0^2 \sin \gamma / e}}{6 \sin \gamma}, & \gamma \neq 0. \end{cases} \qquad (5.5)$$

Then the optimal value of the final cavitation number, the optimal body aspect ratio λ_* and the cavitator radius R_{n*} can be defined from (5.1),(5.4), and (5.5). For example,

$$\sigma_* = \frac{e}{Fr_0^2}\left(\overline{h}_1 + \sqrt{\overline{h}_1^2 - \frac{4\overline{\rho}_b Fr_0^2 \sin \gamma}{3e}} \right), \qquad (5.6)$$

The calculation results of the maximal range by formulae (5.5) and (5.6) are shown in Fig.3 for different motion angles γ. The calculation results with the **SCAV** program (see [21]) are plotted by markers for comparison. The calculations are performed for the model close to the optimal one when $\overline{\rho}_b = 7.8$, L=280 mm, h_0=100 m. For the real supercavitating models, the requirement of the motion stability is obligatory. The motion stability can be checked by the direct computer simulation with the **STAB** program (see [21]). The calculation results with the program for the non-optimal stable model are shown by the dotted line.
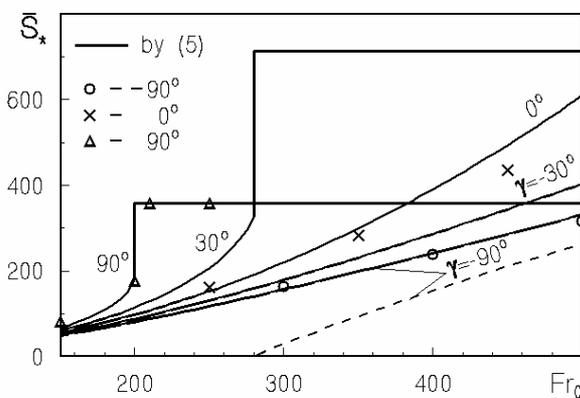

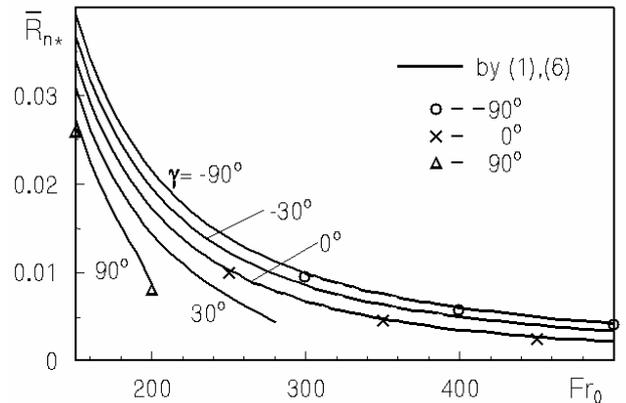**Fig. 3. Optimal range for different angles γ.**

Fig. 4. Optimal cavitator radii

Equation (5.5) shows that for $\gamma > 0$ there is a critical value of the initial Froude number

$$Fr_0^{cr} = \overline{h}_1 \sqrt{\frac{3e}{4\overline{\rho}_b \sin\gamma}} \ . \tag{5.7}$$

If $Fr_0 > Fr_0^{cr}$, equation (5.3) has no solution. This case corresponds to the supercavitating model motion till the water free surface. As a result, the function $\overline{S}_*(Fr_0)$ is discontinuous when $h_0 > 10$ m (see Fig. 3).

The optimal disc cavitator radii, calculated by equations (5.1) and (5.6) are shown in Fig. 4. The calculation results with the **SCAV** program with considering the change of the model aspect ratio according to equations (5.6) and (5.1) are given by markers for comparison.

Analogous investigations have been carried out for the other isoperimetric conditions (the body caliber and volume were fixed instead of the body length), and also for the fixed starting kinetic energy and the fixed starting momentum. In these cases the analytical formulae similar to (5.4)-(5.6) were obtained for the horizontal motion of a supercavitating body (see details in [19]).

When the final depth is fixed, equation (5.3) gives

$$\overline{S} = -\frac{2\overline{\rho}_b Fr_0^2 \overline{U}^2 \ln\overline{U}}{3\overline{h}_2}, \qquad \overline{h}_2 \equiv \frac{10 + h_f}{L} \ . \tag{5.8}$$

Here h_f is the given final depth. Formula (5.4) is still valid, but instead (5.5) and (5.6) the following relations must be used

$$\overline{S}_* = \frac{\overline{\rho}_b Fr_0^2}{3e\overline{h}_2}, \qquad \sigma_* = \frac{2e\overline{h}_2}{Fr_0^2} \ . \tag{5.9}$$

In this case the maximal range does not depend on the angle γ.

For the fixed starting momentum $I_0 = mU_0$, the following formulae have been obtained:

$$\overline{U}_* = e^{-3} \approx 0.0498, \qquad \overline{S}_* = \frac{6a\sigma^{1/6}}{eC_V}, \qquad a = \frac{\rho_b^{2/3} I_0^{1/3}}{\rho[2g(h_f + 10)]^{1/6}}, \qquad C_V = \frac{3^{2/3} \pi^{1/3} \sigma^{4/3}}{4^{2/3}(-\ln\sigma)^{1/3}} \ . \tag{5.10}$$

For the fixed starting kinetic energy $T_0 = mU_0^2/2$, the following formulae have been obtained:

$$\overline{U}_* = e^{-1.5} \approx 0.223, \qquad \overline{S}_* = \frac{3b\sigma^{1/3}}{eC_V}, \qquad b = \frac{\rho_b^{2/3} T_0^{1/3}}{\rho[g(h_f + 10)]^{1/3}} \ . \tag{5.11}$$

In the both cases the optimal value of the final cavitation number σ_* must be as small as possible. For example, when $\sigma_* = 0.01$, equations (5.10) and (5.11) give $\overline{S}_* = 652a$ for $I_0 = const$ and $\overline{S}_* = 152b$ for $T_0 = const$. The analytical formulae for the optimal body volume and mass were obtained as well.

Thus the presented simple analysis makes it possible to obtain the analytical relations for the optimal supercavitating model parameters and the optimal starting parameters. The obtained relations are in good agreement with the more accurate computer calculations.

Gieseke, [18], has calculated the range of 225 m for conical supercavitating projectile with the mass 240 g. The volumetric Reynolds number exceeded the value 10^7 for this body. Calculation by formula (5.11) gives approximately four times greater values of maximal range. This difference is explained by the fact that Gieseke use the non-optimal (conical) body shapes.

Formula (4.3) was used to estimate the maximum range of the unseparated body with the same mass, volume, initial and final velocities as Gieseke's conical projectile . For the unseparated shape the calculations yields 5 times greater value of the range in comparison with the Gieseke's conical body and 25% greater range in comparison with the optimal supercavitating body of [19]. Therefore, the unseparated shapes may compete with the supercavitating bodies in the unsteady motion as well. It must be noted, that the unseparated flow pattern could be better for rather small bodies too.

6. SEPARATION AVOIDING
There are two ways of obtaining the unseparated forms. The simplest one is to use very slender bodies or very thin profiles, which probably ensure no separation independent of the pressure distribution over the surface. The slender 2D and axisymmetric shapes are investigated with the use of the Kochin-Loitsiansky method of local similarity (see, for example, [7]) . A parabolic symmetric profile with the coordinate of the upper surface $Y(x)=4\varepsilon(1-x)x$ and a body of revolution with the same parabolic generatrix were chosen to estimate the value of the thickness parameter ε sufficient for the unseparated flow pattern. The calculations show that the separation occurs for very small values of the thickness parameter ε. For example, even for ε=0.01 the coordinates of the separation point are 0.906 (in the 2D case) and 0.912 (in axisymmetric flow). Thus, the simplest way of avoiding the separation has limited practical interest.

The second way of preventing separation is to use some special forms with appropriate pressure distributions. For example, negative pressure gradients at the body surface are necessary to avoid the separation ([7, 22]). The majority of the researchers consider the minimum of the static pressure coincident with the maximum of the body radius (or with the maximum of the thickness in the 2D case). Moreover, they assume that the pressure gradient is positive after the maximum thickness point. This paradigm was realized in so-called laminarized forms, [22], obtained by shifting the maximum thickness point as far downstream as possible. It would be interesting to investigate if it is possible to have negative pressure gradients after the maximum thickness point too?

Let us investigate more overall question: can flow pressure gradient dp/dx remain negative over the whole body surface?

It has to be answered "NO" for inviscid incompressible fluid. To prove this, it is sufficient to calculate the drag of the axisymmetric body

$$C_x = 2\pi\int_0^1 pR\frac{dR}{dx}dx = -\pi\int_0^1 R^2\frac{dp}{dx}dx ,$$

which must be positive for the negative pressure gradients over the whole surface. On the other hand, the drag must be zero by virtue of the Dalambert paradox.

Thus, another important question arises: can a zone of pressure growth be very short (with negative pressure gradients at the bulk of the surface)?

An example of the axisymmetric body with the negative pressure gradients both before and after the maximum thickness point was presented in [23]. The extent d of the zone with positive pressure gradient was approximately 10% of the total body length. The unseparated flow pattern was achieved in [23] only through the use of the boundary-layer suction.

The problems of decreasing the value d and removing the separation without suction or any other boundary-layer control were investigated in [24-27]. The main results of these papers are presented and discussed in this Section.

The first attempts to solve the problem were made with the use of slender body theory presented, for example, in [12]. The first approximation of this theory yields the following

equation relating the axisymmetric body radius and the pressure coefficient $Cp(x)$ at its surface (see [29, 25]):

$$\frac{d^2R^2}{dx^2} = -\frac{Cp(x)}{ln\,\varepsilon}.$$
(6.1)

Here ε is a small thickness parameter, i.e. the ratio of the maximum body radius to its length.

If the pressure gradient is negative and constant at the surface ($dCp/dx = -\alpha,\ \alpha > 0$), equation (6.1) provides

$$R^2(x) = E\alpha x^2(x-1)\ , \qquad\qquad E = (6ln\,\varepsilon)^{-1}\ .$$
(6.2)

Formula (6.2) shows that normal closed shapes correspond to the negative pressure gradient over the whole surface. Thus, there is no reason to think that the pressure increases downstream of the maximum thickness point. Nevertheless, both the first and the second (see [29]) approximations yield shapes with blunt trailing edges. The developed theory is not valid near these points. The actual pressure distribution differs from the theoretical one, and $Cp(x)$ tends to 1.0. Therefore, a zone with the positive pressure gradient and the separation arise.

To make the trailing edge sharp, discontinuities of dR^2/dx or d^2R^2/dx^2 at some point x_*, $0 < x_* < 1$ are required (see [27]). The discontinuity of the first derivative dR^2/dx means a contour discontinuity, which leads to the separation. According to the first approximation equation (6.1), the discontinuity of the second derivative d^2R^2/dx^2 provides the discontinuity of the pressure. An example of such a solution obtained in [25] has the following form:
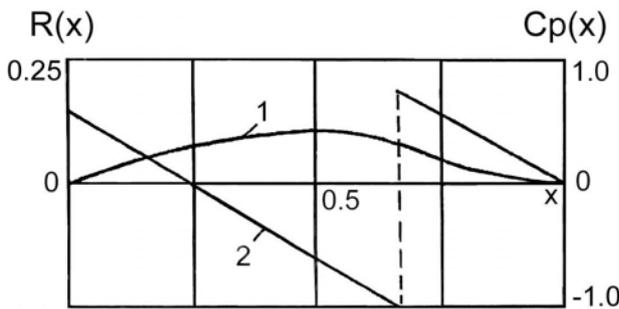
$$Cp(x) = \begin{cases} -ax - 2c, & 0 \le x < x_* \\ -a_1(x-1), & x_* \le x \le 1 \end{cases}$$

$$R^2(x) = \begin{cases} Ex^2(ax+6c), & 0 \le x < x_* \\ Ea_1(x-1)^3, & x_* \le x \le 1 \end{cases}$$
(6.3)

Fig. 5. Shape with a negative pressure gradient.

Here a, a_1, c, E, x_* are constant parameters. The corresponding form (curve 1) and the pressure distribution (curve 2) are shown in Fig. 5. Therefore, the linear theory (equation (6.1)) can yield forms with negative pressure gradients over the whole surface, but a pressure jump at the point $x = x_*$ is required. Slender body theory is not valid near the point $x = x_*$ (because of the discontinuity of d^2R^2/dx^2). This fact provides an explanation for the instant pressure increase, which is impossible in a subsonic flow.

To improve the accuracy and to verify the existence of bodies with a very short region of pressure increase, some exact solutions of the Euler equations have been calculated, which can be applied to non-slender bodies as well (see [24-27]). For this purpose, sources and sinks were placed in the axis of symmetry. Then, the stream function can be defined as follows:

$$\Psi(x,r) = 0.5r^2 - \frac{1}{4\pi}\int_0^1 \frac{(x-\xi)q(\xi)d\xi}{\sqrt{(x-\xi)^2 + r^2}}\ .$$

The first approximation for the intensity of the sources and sinks $q(x)$ can be obtained from equation (6.3) and the relationship $q(x) = \pi dR^2/dx$ (see Cole). The appropriate analytical formula for $\Psi(x,r)$ is presented in [24]. Nevertheless, the region of positive pressure gradient remained rather large with the use of the sources and sinks located on the axis of symmetry.

To make the pressure rise more sharply, additional sinks were distributed on the plane $x = x_*$ inside the body contour.

For some combinations of the sources and sinks, the region of the positive pressure gradient on the body surface can be very small (its length d can be up to 0.3% of the total body length). This result has been achieved by means of numerical experiments: by variation of the parameters a, a_1, c, E, x_* etc., and by seeking the best combination of them.

Some examples of the numerical simulation can be found in [26, 27] and are presented in Figs. 6-8. These shapes show again that the pressure growth downstream of the maximum thickness point is not obligatory. Small dimensions of the pressure increase region encourage belief that these body forms could ensure a flow without separation (first mentioned in [25]).

It should be emphasized that the estimations of the laminar separation point are not valid for such bodies, since they contain zones of large pressure gradients, where both the Kochin-Loitsiansky method of local similarity, and the Prandtl boundary-layer equations are not valid. It is necessary to use the Navier-Stokes equations in these regions or to investigate such bodies experimentally.

It should be mentioned that the body VC ($d = 0.3\%$) shown in Fig.6 is closed. The unclosed shapes V, V-1, V-2 and V-3 with different values of d (from 0.3% to 12%) were expressly calculated and manufactured for wind-tunnel tests. An example is presented in Fig. 7 (see also [26,27]).
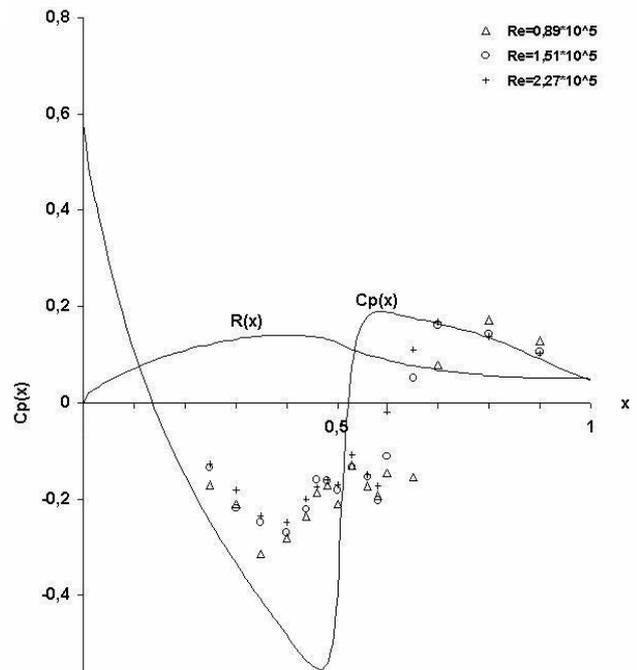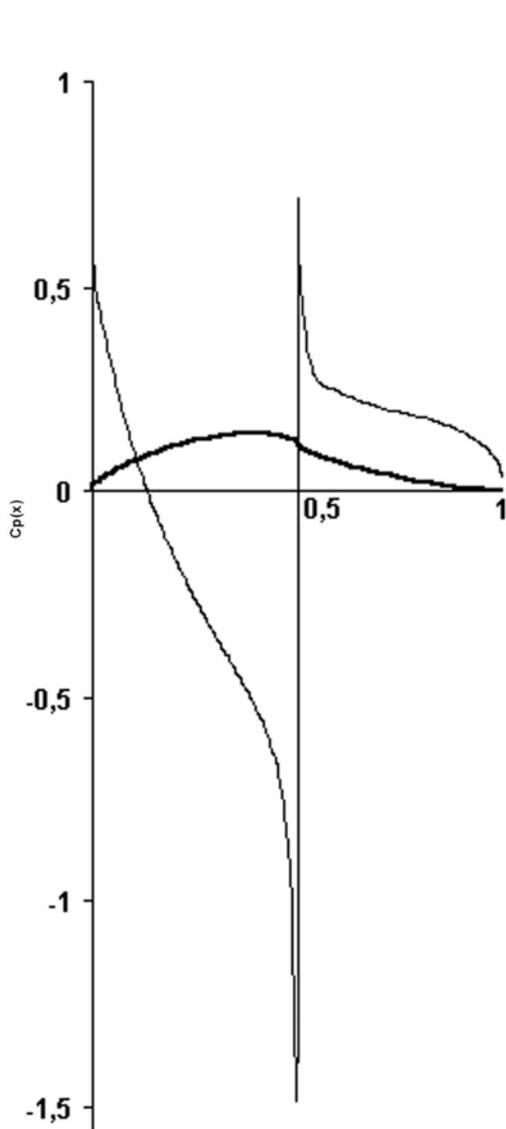

**Fig. 7. Body V-3 (d=12%).
Radius, theoretical and experimental
pressure distributions.**

**Fig.6. Body VC (d=0.3%). Radius and
theoretical pressure distribution.**

The tests were performed for three ranges of the velocity U_∞: 5.7 m/s; 10 m/s; 15 m/s. The measured values of the pressure for different ranges of Re_L are dotted in Figs. 6-8 by markers. The separation occurred at the bodies V, V-1, V-2 and V-3 throughout the velocity range available in the wind tunnel. Nevertheless, the rapid pressure recovery was experimentally confirmed (see Fig. 7). It is neither as large, nor as abrupt as the theoretical one and takes place further downstream. The experimental pressure distributions in Fig. 7 and the wire probe show that the separated regions are short and the re-attachment of the flow takes place.

To obtain a flow pattern without separation, the second series of tests were carried out with the use of small obstacles (rings) on the body surface, [26,27]. An example is presented in Fig. 8. The cross section of the boundary-layer trip rings was either a rectangle or a circle. The main result of the second series of the tests is the absence of the separation for all the bodies V, V-1, V-2 and V-3 at higher flow velocities, for some special positions of the ring. In comparison with the classical tests of Prandtl (see [22]), where a small obstacle on the sphere was used to turbulize the boundary-layer and to reduce the extent of the separated zone, no separation and turbulization were observed in our tests.
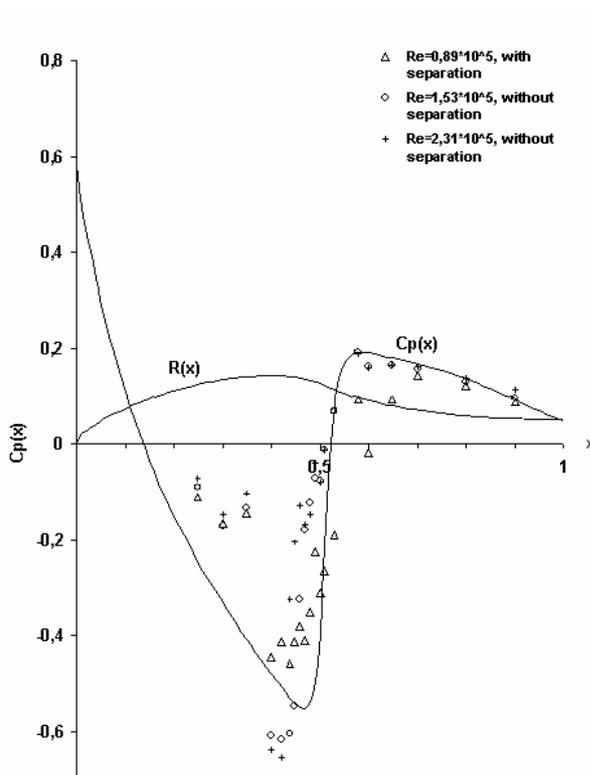

Fig. 8. Body V-3 (d=12%) with the obstacle (ring) on the surface (h=1mm, S=76 mm). Theoretical and experimental pressure distributions.
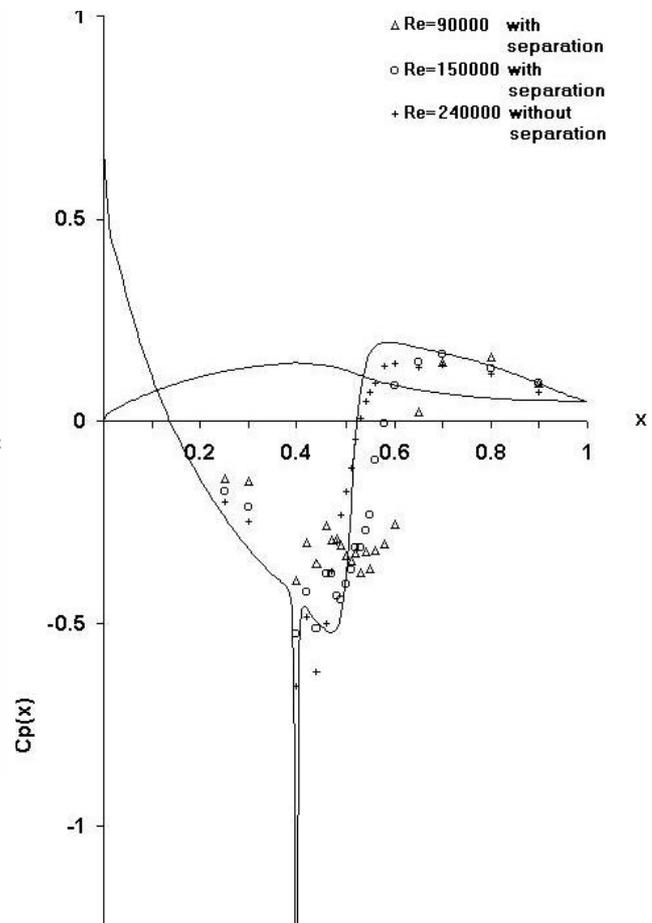
Fig. 9. Unseparated body U-1.

No separation occurred at the body V with a ring throughout the variation interval of the test velocity. The obstacle had a circular cross section with a diameter $\Delta = 1.9$ mm, $S = 120$ mm. The length of the body V was 300 mm; the maximum diameter was 84.96 mm and $d = 0.3$ %. Thus, the presented investigations could be very interesting from the theoretical and practical points of view, since it is easier (and more economical) to use a small ring to

prevent a separation in comparison with the boundary-layer suction or other boundary-layer control methods. Moreover, the necessary size of the obstacle tends to become smaller with increasing Re_L. Before testing the bodies V, V-1, V-2 and V-3 at higher Re it would be interesting to investigate the further "shape possibilities". In particular, can the transformation of the initial forms ensure an unseparated flow pattern without obstacles at low Re numbers, available in the wind tunnel of Kyiv Institute of Hydromechanics? At first, the new axisymmetric shapes obtained with the use of vortex rings inside the body's contour were calculated. The center of these rings was located at the point $x = 0.5$ (in the region of stepwise pressure recovery, see [30]). The axisymmetric shapes W-1, W-2 and W-3 with different signs and intensities of vortices were calculated and tested in the wind tunnel. Unfortunately no unseparated flow pattern was achieved at 90000<Re<300000, see [30]. Further investigations were concerned a new body U-1 (see [30] and Fig. 9). Its shape was obtained by shifting the center of the vortex ring to the point $x = 0.4$. Therefore, the vortex ring was located in the region of maximum thickness inside the body's contour. The shape $V-3$, shown in Figs. 7 and 8 was taken for the initial approximation. In the region $0.38 < x < 0.42$, the radius of the new shape U-1 exceeds the radius of V-3 by no more than 3%. Beyond this zone the shapes U-1 and V-3 practically coincide. Nevertheless, pressure distributions are totally different at $0.38 < x < 0.42$. As shown in Fig. 9 the body U-1 has a sharp pressure minimum at the point $x = 0.4$. This body revealed no separation at higher performance velocities. For smaller Reynolds numbers ($Re_L < 170000$) the separation occurred. This fact can be explained by the influence of the boundary-layer thickness, which exceeds 1.4 % of the
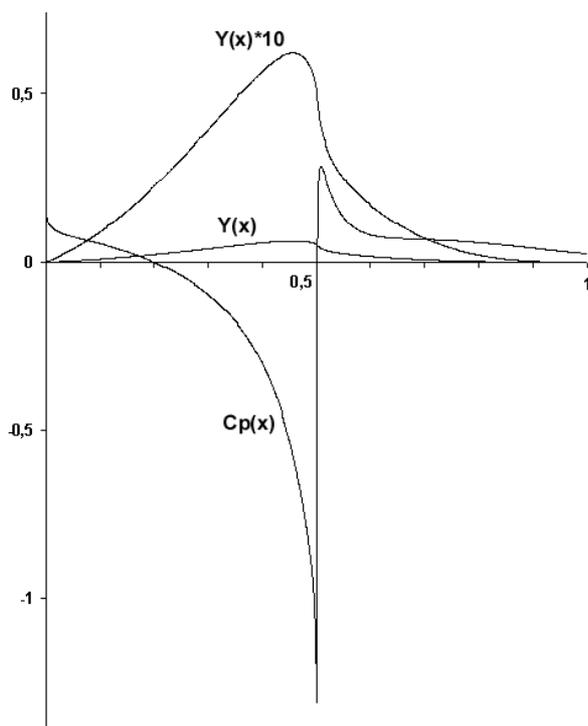

Fig. 10. Symmetric 2D profile P1. Coordinate of upper surface Y(x), Y(x) 10, theoretical pressure distribution.
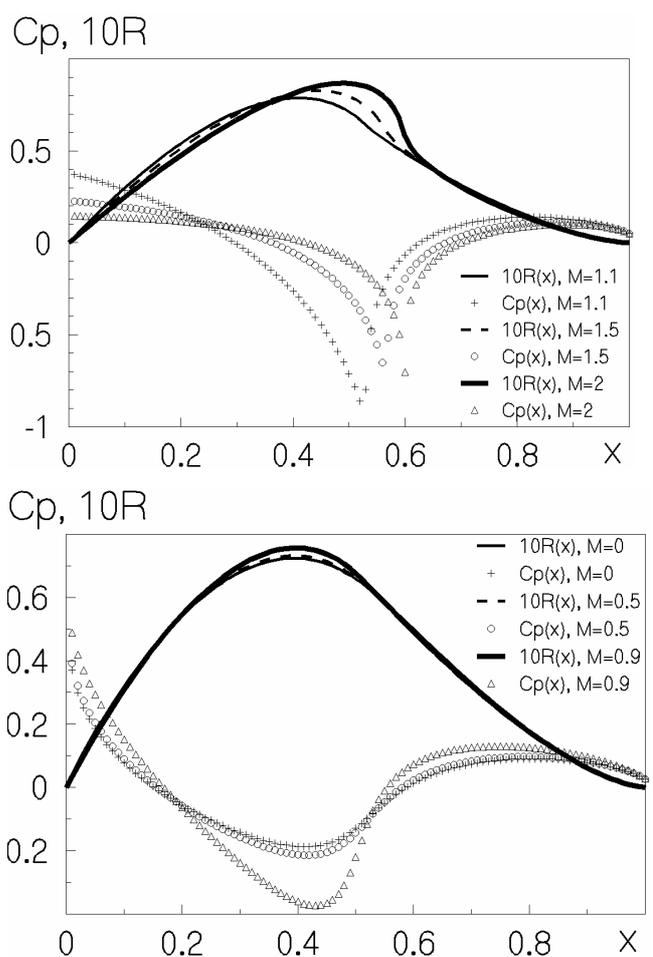
Fig. 11,12. Examples of the unseparated sub- and supersonic axisymmetric shapes

body's radius at $x = 0.38$ and $Re_L < 170000$. The boundary-layer is thinner at higher Reynolds numbers and cannot reduce the influence of the vortex ring. This ring probably prevents the separation by a deflection of the streamlines towards the body surface after the maximum thickness point.

The shapes similar to U-1 are both of theoretical and practical interest. In particular, according to the standard opinion, there must be a separation for the body U-1 at or downstream of the minimum pressure point $x = 0.4$.

Progress in design of the axisymmetric unseparated shapes aroused interest in appropriate 2D forms. Symmetric profiles have been obtained in [31] with the use of the exact solution for an inviscid incompressible fluid. An example is presented in Fig. 10. To make shape peculiarities more visible, the curve $Y(x) \cdot 10$ is also shown in Fig. 10. The thickness ratio equals 6.2% for profile presented in Fig. 10. The value of d is 0.8%. The calculations show that the region with a positive pressure gradient can be very short both for thin and thick profiles. The results presented above can be easily generalized for the compressible flow, since the first approximation equation (6.1) is valid both for a subsonic and for a supersonic flow, [24]. The body radius and the pressure distributions at different values of the Mach number M are calculated and presented in Figs. 11, 12.

7. SEPARATION AND CAVITATON INCEPTION

Cavitation is related to the pressure distribution over the body surface. The point of pressure minimum is usually assumed to be the place of cavitation inception (see, for example, [32]). The boundary-layer separation point is usually located in the same region of minimal pressure (see, for example, [22]). The real processes are more complicated. In particular, they are related to the behavior of the boundary-layer and cavitation nuclei. Nevertheless, the separation can promote the cavitation inception. This fact can be explained as follows: cavitation nuclei need a certain period of time to become unstable, [32]. There are re-circulating flows in the separated zones, therefore the nuclei circulating in these zones have far more time to become unstable and to cause the cavitation in comparison with the nuclei crossing the negative pressure regions without a circulation. The same situation is observed in wakes and submerged jets, where the cavitation centers round the vortex lines, [32]. The paper [33] could be considered as a pure experiment to prove the fact that separation is the main reason of cavitation.Thus, the shapes without separation are of obvious interest as they allow one both to improve the cavitation characteristics and to reduce the hydrodynamic drag.

8. CONCLUSIONS

The volumetric pressure drag of the standard supercavitating bodies and the volumetric friction drag of slender shapes without separation were estimated. The comparison of these values shows that unseparated bodies are preferable for the volumetric Reynolds number $Re_V > 10^7$.

The shapes with negative pressure gradients similar to U-1 provide the unseparated flow pattern. The presented axisymmetric and 2D forms are of considerable practical interest, since only special shaping was used to prevent separation (in comparison with boundary-layer suction or other boundary-layer control methods). Therefore, there is no additional energy supply to avoid separation. According to the Dalambert paradox, all new subsonic shapes have zero pressure drag at higher Reynolds numbers (when the boundary-layer thickness can be neglected). The unseparated flow pattern could prevent cavitation, therefore such shapes could be used for vehicles, moving in water, to improve their cavitation characteristics.

All of these innovative points lead to a system, moving in a gas or liquid, that can supply the drag and noise diminishing and improving the cavitation characteristics.

REFERENCES

[1] Nesteruk I. Drag calculation of slender cones using of the second approximation for created bythem cavities, *Applied Hydromechanics*, 2003, 5(77), No. 1, pp. 42-46. (in Ukrainian).

[2] Nesteruk I. Simulation of axisymmetric and plane free surfaces by means of sources and doublets, *Applied Hydromechanics, Kyiv*, 2003, 5(77), No. 2, pp. 37-44. (in Ukrainian).

[3] Nesteruk I. Some Problems of Axisymmetric Cavity Flows, *Izv. AN SSSR, MFG*, 1982, No. 1, pp. 8-34.

[4] Nesteruk I., Savchenko Yu .M. and Shepetyuk B.D. Estimation of the cavitator curvature influence on the pressure drag for the axisymmetric supercavitating flow pattern, *Reports of the Ukrainian Academy of Sciences*, 2003, № 8, pp. 59-64. (in Ukrainian).

[5] Greiner L. *Underwater missile propulsion.* – Compass Publications, Inc., (1967).

[6] Hoerner S.F. *Fluid-dynamic drag*, Midland Park, N.J. (1965).

[7] Loitsiansky L.G. *Mechanics of liquid and gas*, Moscow: Nauka,(1978).

[8] Lutz Th., Wagner S. Drag Reduction and Shape Optimization of Airship Bodies, *Journal of Aircraft*, 1998, v. 35, No. 3, pp. 345-351.

[9] Nesteruk I., Drag Coefficient Calculations of Slender Axisymmetric Subsonic Bodies, *Applied Hydromechanics, Kyiv*, 2002, No. 1, pp. 44-49. (in Ukrainian).

[10] Nesteruk I. Hydrodynamic drag estimations for slender axisymmetric unseparated subsonic forms, *Reports of the Ukrainian Academy of Sciences*, 2002, No. 7. –P. 54-60. (in Ukrainian)

[11] Nesteruk I. Peculiarities of Turbulization and Separation of Boundary-Layer on Slender Axisymmetric Subsonic Bodies, *Naukovi visti, NTUU "Kyiv Polytech. Inst."* , 2002, No. 3, pp. 70-76. (In Ukrainian).

[12] Cole J.D. *Perturbation Methods in Applied Mathematics*, Blaisdell Publishing Company (1968).

[13] Hansen R.J., Hoyt J.G. Laminar-To-Turbulent Transition on a Body of Revolution with an Extended Favorable Pressure Gradient Forebody, 1984, V. 106, pp. 202-210.

[14] Dodbele S.S., Van Dam C.P., Vijgen P.M., Holms B.J. Shaping of Airplane Fuselages for Minimum Drag, *Journal of Aircraft*, 1987, V. 24, No 5, pp. 298-304.

[15] Zedan M.F., Seif A.A. and Al-Moufadi S. Drag Reduction of Fuselages Through Shaping by the Inverse Method, *Journal of Aircraft*, 1994, V. 31, No. 2, pp. 279-287.

[16] Lorant M., 1968, "Investigation into High-Speed of Underwater Craft", *Nautical Magazine*, 1968, v. 200, No.5, pp. 273-276.

[17] Putilin S.I. Some features of dynamics of supercavitating models. *Applied hydromechanics*, 2000, Vol.2 (74), No.3, pp. 65-74.

[18] Gieseke T.J. Toward an optimal weapon system utilizing supercavitating projectiles. *Int. Conference on Cavitation "Cav2001"*, 2001, Pasadena, USA, SessionB3.002.

[19] Nesteruk I., Semenenko V.N. Optimization problems for supercavitation motion of axisymmetrical bodies on inertia. *Applied hydromechanics*, 2006, Vol. 8 (80), No.1, pp. 51-59 (in Ukrainian).

[20] Nesteruk I., Savchenko Yu .M. Semenenko V.N., 2006. Range optimization for supercavitating motion on inertia. *Reports of Ukrainian Academy of Sciences*, 2006, No. 8, pp. 57-66. (in Ukrainian).

[21] Savchenko Yu.N., Semenenko V.N., Putilin S.I. and others. Designing the high-speed supercavitating vehicles. *Int. Conference On Fast Sea Transportation (FAST'2005)*, June 2005, St.Peterburg, Russia.

[22] Schlichting H. *Entstehung der Turbulenz, Handbuch der Physik*, v. VII/1, pp. 341-450 (1959).

[23] Goldschmied F.R. Integrated Hull Design, Boundary-Layer Control and Propulsion of Submerged Bodies: Wind-Tunnel Verification, *AIAA/SAE/ASME 18-th Joint Propulsion Conference*, 1982, Cleveland

[24] Nesteruk I. Body forms of minimal drag. *Reports of Ukrainian Academy of Sciences.*, 1989, A, **4**, 57-60.

[25] Nesteruk I. Some Problems of Slender Axisymmetric Cavitator Dynamics, *Transactions of Boundary Problems Seminar in Kazan University*, 1990, **24**, pp. 187-197 (In Russian).

[26] Nesteruk I. Experimental Investigation of Axisymmetric Bodies with Negative Pressure Gradients, *Aeronautical Journ.*, 2000, **104**, pp. 439-443.

[27] Buraga O.A., Nesteruk I.G., and Shepetyuk B.D. Subsonic Axisymmetric Forms with a Pressure Jump on the Surface. *Naukovi visti, NTUU "Kyiv Polytech. Inst."*, 2001, **1(15)**, pp. 90-99. (In Ukrainian).

[28] Garabedian P.R. Calculation of axially symmetric cavities and jets. *Pac. J. Math.*, 1956, Vol.6, No.4, pp. 611-684.

[29] Nesteruk I. The Slender Axisymmetric Cavity Form Calculations Based on the Integral-Differential Equation, *Izv.AN SSSR, MZhG*, 1985, **5**, pp. 83-90. (in Russian.).

[30] Nesteruk I. Search for Axisymmetrical Subsonic Forms without Separation, . *Reports of Ukrainian Academy of Sciences*, 2002, **5**, pp. 59-64. (in Ukrainian).

[31] Nesteruk I. Plane Subsonic Forms with Negative Pressure Gradients on the Surface, . *Reports of Ukrainian Academy of Sciences*, 2001, **9**, p. 63-68. (In Ukrainian).

[32] Knapp R.T., Daily J.W., and Hammitt F.G. *Cavitation*, McGRAW HILL Book Company, (1970).

[33] Takahashi S., Washio S., Uemura K., Okazaki A. Experimental study on cavitation starting at and flow characteristics close to the point of separation, 2003, No. Cav03-OS-3-003.